Research Square

Preprints are preliminary reports that have not undergone peer review.
They should not be considered conclusive, used to inform clinical practice,
or referenced by the media as validated information.

Synthesis of Cu-Se-O compounds and p-type thin films obtained by pulsed laser deposition and their optoelectronic properties

J. A. Melchor-Robles
Centro de Investigación y de Estudios Avanzados del Instituto Politécnico Nacional
Jacobo Martínez-Reyes
jacobo.martinez.r@cinvestav.mx

Centro de Investigación y de Estudios Avanzados del Instituto Politécnico Nacional
Edgar David Peduzine Orozco
Popular University of Cesar
T. N. Domínguez Mendoza
Instituto Politécnico Nacional
K. E. Nieto-Zepeda
Instituto Politécnico Nacional (ESIAZ-IPN), Unidad Profesional Adolfo L´ opez Mateo
F. de Moure-Flores
Autonomous University of Queretaro
María Luz Olvera-Amador
Centro de Investigación y de Estudios Avanzados del Instituto Politécnico Nacional
Miguel Ángel Meléndez Lira
Centro de Investigación y de Estudios Avanzados del Instituto Politécnico Nacional

Research Article

Keywords: Copper oxychalcogenides, ball milling, p-type semiconductor, pulsed laser deposition, nanostructured thin films

Posted Date: September 16th, 2026

DOI: https://doi.org/10.21203/rs.3.rs-10844092/v1

License: This work is licensed under a Creative Commons Attribution 4.0 International License.
Read Full License

Additional Declarations: No competing interests reported.

Abstract

In this work it is reported the successful deposition of Cu–Se–O thin films by pulsed laser deposition. Precursor powders were obtained by high-energy ball milling employing CuO and elemental selenium, processed for 2, 4, and 6 h. X-ray diffraction and Raman spectroscopy indicate the formation of multiple Cu–Se–O crystalline phases, with phase evolution as a function of milling time. Raman spectroscopy results indicate variations in the Cu–Se–O vibrational features after the powders are deposited as thin films. The films exhibit a morphology that varies depending on the precursor powder, progressing from fragmented nanosheets to interconnected nanorods and semispherical particles. The film obtained using the powder milled for 6 h exhibits a single-phase $Cu_4O(SeO_3)_3$ structure, with crystallite sizes ranging from approximately 21.7 to 32.8 nm. Optical measurements indicate an optical band gap in the range of 1.8–2.0 eV. Room-temperature photoluminescence measurements show emissions in the near-band-edge region, with a broad emission centered at approximately 1.78 eV for F1-PLD and more defined emissions around 1.95–1.97 eV for F2-PLD and F3-PLD. Electrical measurements indicate p-type conductivity with carrier mobilities reaching up to 419.6 $cm^2/V{\cdot}s$ and carrier concentrations ranging from 1.07×10^{16} to 1.86×10^{21} cm^{-3}. The use of high-energy ball-milled Cu–Se–O powders as precursors for PLD allows the preparation of Cu–Se–O thin films, with the resulting materials being of interest for semitransparent p-type oxychalcogenide applications in optoelectronics.

1 Introduction

Copper-based chalcogenide and oxychalcogenide materials have attracted significant attention in recent decades as potential p-type semiconductors, particularly for the development of optically transparent or semitransparent materials for optoelectronic applications [1]. Unlike conventional oxides, in which the valence band is dominated by highly localized O 2p orbitals, Cu^+/Cu^{2+}-based systems exhibit hybridization between Cu 3d orbitals and chalcogen p states. This interaction promotes enhanced valence-band dispersion and may facilitate more efficient hole transport [1–3].

Among metallic chalcogenides, copper sulfides have been extensively studied due to their intrinsic p-type semiconducting behavior and their pronounced crystallographic polymorphism as a function of stoichiometry and synthesis conditions. This structural versatility leads to phases with distinct optoelectronic properties, enabling their exploration in applications such as photocatalysis, plasmonics [4], photothermal therapy [5], solar energy conversion [6], optical filters [7], and superionic materials [8–9]. Within this family, copper-rich (Cu_2S) and sulfur-rich (CuS) systems can be distinguished, where the Cu/S ratio influences both direct and indirect band gap values, typically reported in the range of approximately 1.2–1.5 eV [10].

This compositional dependence has motivated research on other chalcogenides, particularly the Cu–Se system, which occurs naturally in several minerals with complex crystal structures. Representative examples include berzelianite (α-Cu_{2-}□Se), umangite (Cu_3Se_2), and klockmannite (CuSe), among others [11–12]. The formation of these Cu–Se compounds is influenced by system enthalpy and synthesis

temperature, often leading to metastable phases and polymorphic transitions. For example, Cu_2Se adopts a face-centered cubic structure at high temperatures, whereas at lower temperatures the α-Cu_2Se phase stabilizes in the Fm3̄m space group [13].

Similarly, CuSe exhibits several polymorphs (α, β, and γ) with hexagonal, trigonal, and orthorhombic symmetries, while $CuSe_2$ may crystallize in a marcasite-type structure (Pnnm) or transform into a cubic pyrite-type phase at elevated temperatures. This structural diversity has resulted in discrepancies in phase identification and space-group assignments in the literature, reflecting the intrinsic complexity of the Cu–Se system [11, 14–15]. These characteristics have motivated the exploration of more complex systems in which additional elements, such as oxygen, are incorporated into copper chalcogenide frameworks.

In recent years, attention has shifted toward copper oxides and oxychalcogenides, where oxygen incorporation can modify crystal structure, copper oxidation state, and electronic properties. The incorporation of oxygen can therefore provide additional flexibility in controlling the crystal structure, copper oxidation state, and electronic properties of these materials. However, the relationship between crystal structure, microstructure, and optoelectronic behavior in Cu–O–Se systems remains not fully understood, particularly for materials obtained through mechanochemical synthesis routes. Although several Cu–Se and Cu–Se–O compounds have been individually investigated, studies correlating the structural evolution of mechanically activated precursor powders with the phase evolution and optoelectronic properties of Cu–Se–O thin films deposited by PLD remain limited. Understanding this relationship is important for controlling phase formation and evaluating the potential of Cu–Se–O oxychalcogenides as p-type semitransparent thin-film materials.

Based on these considerations, the objective of the present work is to investigate the ball-milling synthesis of copper oxyselenides within the Cu–Se–O system, with particular attention to structures possibly related to $CuSeO_3$ and $Cu(SeO_3)$, and their subsequent deposition as thin films by pulsed laser deposition. The influence of precursor milling time on the phase composition, microstructure, morphology, optical response, and electrical properties of the resulting films is examined. In particular, the structural and optoelectronic characteristics are evaluated to assess the potential of Cu–Se–O thin films as semitransparent p-type materials for optoelectronic applications.

2 Experimental methodology

2.1 Material synthesis

Polycrystalline Cu–Se–O systems were synthesized by ball milling (BM) using precursor powders of copper oxide (CuO, 3.5 g, 99.99%, Sigma-Aldrich) and elemental selenium (Se, 3.9 g, 99.99%, Sigma-Aldrich). Mechanical milling was carried out in a Fritsch PULVERISETTE 7 planetary mill operating at 400 rpm under reversible rotation. The process consisted of 5 min milling cycles followed by 5 min rest periods to minimize excessive temperature rise and promote homogeneous mixing [16–17]. Milling

times of 2, 4, and 6 h were investigated, and the resulting powders were labeled P1-BM-2H, P2-BM-4H, and P3-BM-6H, respectively. The milled powders were subsequently compacted into cylindrical pellets with a diameter of 7 mm by applying 15 tons for 15 min using a hydraulic press. The resulting pellets exhibited sufficient mechanical stability for use as targets in pulsed laser deposition (PLD). Thin films were deposited from pellets prepared using powders milled for 2, 4, and 6 h (P1-BM-2H, P2-BM-4H, and P3-BM-6H). The deposited films were identified as F1-PLD, F2-PLD, and F3-PLD, respectively, where the sample ID indicates the precursor powder employed for target preparation. Depositions were carried out onto soda–lime glass substrates using an EKSPLA Nd:YAG laser operating at a wavelength of 1064 nm. A total laser energy of approximately 270 J was delivered during the deposition process, corresponding to 300 pulses (0.9 J per pulse), and was measured using a PowerMax PC energy meter (Coherent). The substrate temperature was maintained at 350°C during deposition, which was carried out for 5 min with a target-to-substrate distance of 5 cm.

Following deposition, all films were subjected to thermal annealing at 530°C under a nitrogen atmosphere. The samples were encapsulated in a semi-hermetic graphite crucible and annealed in a horizontal furnace for 5 min under a continuous nitrogen flow of 1 L/min to maintain a controlled thermal environment.

2.2 Material characterization

The crystal structure of the samples was analyzed using a PANalytical X'Pert PRO diffractometer equipped with a Cu Kα radiation source (λ = 0.154178 nm), operated at 45 kV and 40 mA. The diffraction patterns were recorded in the 2θ range of 5–80 ° for films and 15–80 ° for powders, with a step size of 0.02° and a scanning rate of one degree per minute. Phase identification was performed using the HighScore Plus software (PANalytical) and reference data from the International Centre for Diffraction Data (ICDD) database [18]. Raman spectra were obtained using a Jobin-Yvon micro-Raman system, employing the 632 nm wavelength of He-Ne laser as excitation source. The morphology of the samples was examined by SEM using a JEOL JSM-7401F microscope. The accelerating voltage was maintained between 18 and 25 kV, with a beam current of approximately 15 nA. Elemental composition of the different Cu-Se-O systems was determined by EDS. Optical transmittance was measured by ultraviolet–visible (UV–Vis) spectroscopy using a Jasco-670 spectrophotometer over the wavelength range of 200–1100 nm, with a spectral resolution of 1 nm. The photoluminescence (PL) response was measured using a SPEX 3247 spectrometer with a 488 nm excitation laser.

Electrical characterization was performed using a Hall effect measurement system (HMS-3000), from which key transport parameters carrier concentration, mobility, and resistivity were obtained.

3 Results and Discussion

3.1 Cu-Se-O powders.

Figure 1 presents the XRD patterns together with the Rietveld refinements using HighScore Plus software (Malvern PANalytical) of the Cu–Se–O powders synthesized by high-energy ball milling for 2, 4, and 6 h. Progressive changes in the diffraction patterns are observed with increasing milling time, indicating a continuous structural evolution of the Cu–Se–O system. The refinement provides quantitative information on the phase composition, crystallite size, and lattice strain, as summarized in Table 1[19].

The P1-BM-2H sample is mainly composed of Cu_2O (89.23 wt.%), together with a minor amount of elemental Se (10.27 wt.%), indicating that the mechanochemical reaction is still at an early stage after 2 h of milling. After 4 h of milling (P2-BM-4H), the elemental Se phase disappears and the $CuSe_2$ phase emerges, accounting for 14.58 wt.% of the sample, while Cu_2O remains the predominant phase. This result indicates the onset of the mechanochemical reaction between the precursor materials. For the P3-BM-6H sample, the $CuSe_2$ phase becomes dominant (72.3 wt.%), whereas the Cu_2O content decreases to 19.0 wt.%. Additionally, the appearance of $CuSeO_3$ (8.7 wt.%) indicates the formation of a more complex Cu–Se–O oxychalcogenide system after prolonged milling. These results demonstrate a progressive phase evolution driven by the increase in milling time [20–22].

The quantitative phase analysis obtained from the Rietveld refinement, together with the crystallite size and lattice strain values, is summarized in Table 1. These results indicate that increasing the milling time modifies not only the phase composition but also the microstructural characteristics of the powders.

Table 1
XRD parameters of the Cu-Se-O powders, obtained from XRD analysis.

Id. Sample	Size (nm)	Strain (%)	Phase	Reference code ICCD	Quantification (%)
P1-BM-2H	9.2	0.224	Cu_2O	01-078-2076	89.23
			Se	01-073-0465	10.27
P2-BM-4H	37.47	0.254	Cu_2O	01-078-2076	85.42
			$CuSe_2$	01-071-0047	14.58
P3-BM-6H	16.48	0.230	Cu_2O	01-078-2076	19.0
			$CuSe_2$	01-071-0047	72.3
			$CuSeO_3$	00-031-0479	8.7

Figure 2 shows Raman spectra of Cu-Se-O powders synthesized by BM at different milling times. The P1-BM-2H powder exhibits Raman bands centered at 427 and 711 cm^{-1}, indicating the presence of common Cu–Se–O structural features, mainly related to Se–O stretching and Cu–O vibrational modes [23]. For the P2-BM-4H sample, the Raman spectrum is dominated by bands at ~ 428 and 708 cm^{-1}, accompanied by additional low-intensity features at ~ 187, 257, and 490 cm^{-1} [24]. The emergence of these modes

reflects an increase in local vibrational complexity, which can be attributed to mechanically induced disorder and the coexistence of multiple Cu–Se–O environments. In the case of P3-BM-6H, the Raman bands become better defined and show a slight shift toward ~ 429 and 705 cm^{-1}, while weaker modes are detected at ~ 188, 257, 450, 490, and 708 cm^{-1} [24–25].

Figure 3 shows the SEM micrographs of Cu–Se–O powders obtained by BM at different milling times. In general, particle agglomerates with micrometer-scale dimensions are observed, together with semispherical particles distributed over their surface, likely formed during the mechanosynthesis process. The average particle size was measured from the SEM micrographs using ImageJ software. For 2 h of milling (P1-BM-2H, Fig. 3A), a main aggregate composed of irregularly shaped particle agglomerates with characteristic sizes on the order of ~ 12 µm is observed. A higher magnification image of a selected region (Fig. 3A1) shows semispherical particles with approximate diameters of ~ 350 nm located on the surface of these agglomerates. Increasing the milling time to 4 h (P2-BM-4H, Fig. 3B), the surface morphology evolves toward agglomerates with a more homogeneous particle distribution. Although irregular shapes are still present, a reduction in average size to approximately ~ 1 µm is observed, together with secondary particles of about ~ 250 nm on the surface (Fig. 3B1), indicating a progressive fragmentation and refinement process. After 6 h of milling (P3-BM-6H, Fig. 3C), agglomerates composed of more uniform particles with average sizes close to ~ 100 nm are observed, as shown in greater detail in Fig. 3C1. Overall, increasing the milling time promotes particle size reduction and morphological homogenization, favoring the formation of powders with particle sizes below ~ 100 nm [26–27].

The elemental chemical analysis obtained by EDS (Table 2) reveals a compositional variation of the Cu–Se–O system as a function of mechanical milling time. The P1-BM-2H sample is dominated by Cu (40.69 at. %) and Se (37.57 at. %), with a lower oxygen content (21.74 at. %), suggesting a limited degree of oxidation during the early stages of the BM process. As the milling time increases to 4 h (P2-BM-4H), an increase in the Cu content (49.63 at. %) is observed, accompanied by a relative decrease in Se (31.26 at. %) and O (19.10 at. %). This behavior may be associated with elemental redistribution induced by mechanical activation and the possible formation of Cu-rich environments. In contrast, the P3-BM-6H sample exhibits a higher oxygen concentration (36.44 at. %), together with comparable amounts of Cu (33.28 at. %) and Se (30.28 at. %). This composition is closer to the expected range for Cu–Se–O systems. This trend may be related to particle size reduction and the associated increase in surface area promoted by prolonged milling, which can facilitate oxidation and the formation of oxide and oxyselenide phases, in agreement with the XRD results.

Table 2
Atomic concentrations of Cu, O, and Se in the Cu-Se-O powders, obtained from EDS analysis.

Id. Sample	Cu (At. %)	O (At. %)	Se (At. %)
P1-BM-2H	40.69	21.74	37.57
P2-BM-4H	49.63	19.10	31.26
P3-BM-6H	33.28	36.44	30.28

3.2 Thin films of Cu–Se–O

Figure 4 presents the XRD patterns together with the Rietveld refinements (X' pert HighScore Plus) of the Cu–Se–O thin films deposited by PLD using targets prepared from powders milled for different times. The diffraction patterns reveal a progressive structural evolution as a function of the precursor powder. Quantitative phase analysis, summarized in Table 3, indicates significant changes in the phase composition, crystallite size, and lattice strain. The F1-PLD film exhibits a multiphase structure composed predominantly of Cu_2O (56.5 wt.%), together with Cu_2Se (20.03 wt.%), $CuSeO_3$ (7.0 wt.%), and $Cu(SeO_3)$ (16.2 wt.%). In the F2-PLD film, the Cu_2O fraction increases to 77.4 wt.%, while the Cu_2Se content decreases to 8.3 wt.% and the $CuSeO_3$ fraction increases to 14.3 wt.%; in addition, the $Cu(SeO_3)$ phase is no longer detected. These changes indicate a progressive structural evolution toward a Cu–Se–O oxychalcogenide system with increasing milling time of the precursor powder. A markedly different behavior is observed for F3-PLD, where the diffraction pattern is refined as a single $Cu_4O(SeO_3)_3$ phase (ICDD 00-046-0794). This structural transformation is accompanied by an increase in the average crystallite size from approximately 22 nm to 33 nm, whereas the lattice strain remains within the same order of magnitude for all films. Overall, these results suggest that prolonged mechanical activation of the precursor powders suggesting that prolonged milling of the precursor powders modifies the phase assemblage transferred during PLD and favors the stabilization of the $Cu_4O(SeO_3)_3$ phase [20–21, 28–29].

Table 3
XRD parameters of the Cu-Se-O thin films, obtained from XRD analysis.

Id. Sample	Size (nm)	Strain (%)	Phase	Reference code ICCD	Quantification (%)
F1-PLD	21.9	0.005	Cu_2O	01-078-2076	56.5
			Cu_2Se	01-088-2044	20.03
			$CuSeO_3$	00-031-0479	7.0
			$CuSeO_3$	00-048-0375	16.2
F2-PLD	21.68	0.0043	Cu_2O	01-078-2076	77.4
			Cu_2Se	01-088-2044	8.3
			$CuSeO_3$	00-031-0479	14.3
F3-PLD	32.79	0.0054	Cu4O(SeO3)3	00-046-0794	100

The XRD patterns of the Cu–Se–O thin films show that the phases present in the system are not limited to a single structural arrangement. Instead, the reflections can be associated with configurations commonly reported for orthorhombic Pnma-type structures, where Cu^{2+} ions occupy nonequivalent sites coordinated by distorted CuO_5 units, while Se^{4+} species are arranged in trigonal environments [29–30]. These local configurations have been related in previous studies to the formation of copper vacancies under oxygen-rich conditions, which could help explain the presence of more than one oxoselenate phase in the films. In terms of the Cu–Se–O ternary diagram, this behavior is consistent with regions where several phases may coexist rather than a single stable compound. It is also worth considering that the structural features observed here may be influenced by the mechanical milling stage used to prepare the targets. This process introduces additional energy into the system and can lead to local rearrangements that are not necessarily uniform. As a result, it is reasonable to expect the presence of both orthorhombic and triclinic (anorthic) configurations, as has been reported for related systems covering a wide range of space groups [31].

A similar interpretation is supported by the chemical potential calculations of the Cu–Se–O system performed with the Chesta software (Fig. 5). These calculations show that phases such as $CuSe_2$, $CuSeO_3$, Cu_2SeO_3, CuO, and Cu_2O can appear within relatively close stability regions. In particular, $CuSeO_3$ is located within a comparatively narrow stability range, which suggests that even small variations in oxygen chemical potential may affect its formation. This observation is in line with the phase coexistence seen in the XRD results and supports the idea that the system does not evolve toward a single phase but rather toward a mixture of related structures [30, 32].

Figure 6 shows Raman spectra of Cu–Se–O thin films deposited by PLD. In the low-frequency region, bands located around ~ 185 and ~ 260 cm^{-1} can be associated with collective lattice vibrations of the Cu–Se network, in agreement with the Eg modes reported by Ibrahim Garba Shitua and Khalida Mubeen et al. [24] (~ 185.7 cm^{-1}) in CuSe nanoparticles and nanocomposites, as well as by Lingzhi L. et al. [33] (~ 260 cm^{-1}) in CuSe nanosheets. In the intermediate-frequency region, bands observed at ~ 429, ~450, and ~ 489 cm^{-1} are attributed to mixed Cu–Se-O vibrations and O–Se–O bending modes. This assignment is consistent with reports by A. H. Goldan et al. [23], who identified modes around ~ 450 cm^{-1} in amorphous selenium, and with studies by Yaran Zhao and Yilin Denghan et al. [25, 34], where bands near ~ 490 cm^{-1} are associated with Cu–O vibrations in copper oxides. At higher frequencies, bands detected at ~ 603 and ~ 708 cm^{-1} are mainly related to Se–O stretching modes. Similar features have been discussed in the work of Ray L. [35], who attributed a mode near ~ 710 cm^{-1} to vibrations of the $(SeO_3)^{2-}$ group, as well as in reports of bands around 600–610 cm^{-1} associated with Cu–O stretching in copper oxides. Overall, the Raman results obtained here are consistent with previous reports [23–25, 35] and allow a reasonable assignment of the vibrational modes associated with the polymorphic nature of the Cu–Se-O system, providing complementary information about its local structure.

The morphology of Cu–Se–O thin films deposited by PLD shows a clear microstructural variation that appears to depend on the characteristics of the precursor powders, as shown in Fig. 7. The F1-PLD film, derived from the P1-BM-2H powder (Fig. 7A), presents a heterogeneous surface characterized by the coalescence of nanoparticles with sizes ≤ 100 nm, together with fragmented nanosheets (nanoflakes) with thicknesses on the order of ~ 30 nm and lengths of approximately ~ 200 nm. This morphology suggests an early stage of anisotropic growth, possibly influenced by limited adatom surface mobility and by residual energy inherited from the BM process, which may favor two-dimensional nucleation and the formation of lamellar structures. For the F2-PLD film, obtained from the P2-BM-4H powder (Fig. 7B), a noticeable change in morphology is observed. The surface is dominated by nanoparticles from which interlaced nanorods emerge, with average lengths of ~ 800 nm and thicknesses in the range of 40–50 nm. This evolution suggests that the nanosheets observed in the previous sample may act as structural precursors that reorganize into a one-dimensional growth morphology. Such behavior can be associated with surface diffusion processes and coalescence effects, as well as with local compositional variations within the Cu–Se–O system. In the case of the F3-PLD film, derived from the P3-BM-6H powder (Fig. 7C), a reduction of the previously observed anisotropic features is evident, leading to a more homogeneous surface mainly composed of semispherical nanoparticles with average sizes of ~ 70 nm, together with some dispersed agglomerates of approximately ~ 250 nm (Fig. 7C1). This behavior suggests a tendency toward surface energy reduction through particle rearrangement and agglomeration, resulting in more compact morphologies. Under these conditions, the nanorods appear less prominent, giving way to structures with lower aspect ratio [36–37].

The elemental composition of the Cu–Se–O thin films obtained by EDS is summarized in Table 4. For the F1-PLD film, the atomic fractions are Cu (7.80 at. %), O (77.07 at. %), and Se (15.12 at. %), with oxygen being the dominant element. For the F2-PLD film, the composition shows Cu (4.35 at. %), O (88.21 at. %), and Se (7.44 at. %), indicating an increase in oxygen content and a decrease in both Cu and Se compared

to the previous sample. In the case of the F3-PLD film, the atomic composition is Cu (7.46 at. %), O (84.55 at. %), and Se (7.99 at. %), showing a similar Cu content to F1-PLD, while Se decreases and oxygen remains the predominant element [38–40].

Table 4
Results of EDS analysis of deposited thin films.

Id. Sample	Cu (At. %)	O (At. %)	Se (At. %)
F1-PLD	7.80	77.07	15.12
F2-PLD	4.35	88.21	7.44
F3-PLD	7.46	84.55	7.99

3.3 Optical and electrical properties of Cu–Se–O thin films

Optical transmittance was measured for the Cu–Se–O thin films within the 300–1100 nm range (Fig. 8). In the case of the F1-PLD sample, the spectrum shows a clear drop in transmittance around 500 nm, with values in the visible region remaining close to 10%. The response of the other films differs noticeably. For F2-PLD and F3-PLD, transmittance in the visible range is considerably higher, typically between 50 and 60%. At the same time, the absorption edge is no longer located at 500 nm, but appears shifted toward longer wavelengths, near 550 nm.

The optical band gap of the Cu–Se–O thin films was determined from Tauc plots (Fig. 9) constructed from the measured absorbance spectra. The analysis was performed assuming an indirect allowed transition according to the Tauc relation $\left(\alpha\, h\nu\,\right)^{1/2} = A(h\nu\, - E_g\right)$ [41–42], giving values in the range of 1.8–2.0 eV. This range falls within what has been described for copper oxide-related systems [43]. In previous work, Garba et al. [44] described a shift of Eg from 1.80 to 2.10 eV as particle size decreased, linking this behavior to structural modifications at the nanoscale. For copper selenide-based materials, however, lower values have been reported. For example, Krishnan et al. [45] indicated that Cu_2Se and Cu_2−xSe nanostructures typically show band gaps between 1.41 and 1.52 eV, which has been associated with the contribution of selenium. A somewhat different trend was described by Ali et al. [46], where Eg decreases gradually after thermal treatment, from 2.1 eV to 1.9 eV as the temperature increases. Along with this change, variations in optical response were also noted, including lower transmittance and reflectance and a higher absorption coefficient. In that context, the narrowing of the band gap has been linked to an increase in absorption [47–48]. Additional values reported by Lee et al. [49] place the band gap of Cu_2Se close to 2.2 eV, while elemental Se is found near 1.9 eV, with estimated values around 2.15 eV and 1.79 eV, respectively.

PL measurements were carried out in the 500–800 nm (2.4–1.2 eV) range using a 488 nm excitation source (Fig. 10). In the case of F1-PLD, the emission is relatively broad and centered at approximately

1.78 eV. The PL spectrum was fitted with a single Gaussian component, indicating that the emission is dominated by a single radiative process. The broad emission profile is characteristic of polycrystalline semiconductors, where structural disorder and local variations in the electronic environment contribute to spectral broadening. For F2-PLD, the emission shifts toward higher energies and the PL spectrum was fitted with two Gaussian components centered at approximately 1.95 and 1.97 eV. Both components exhibit comparable intensities, although the 1.97 eV emission is slightly more intense than the 1.95 eV component. A similar behavior is observed for F3-PLD, where the Gaussian components remain at approximately the same energy. However, the relative intensity of the 1.97 eV component increases markedly, becoming nearly twice that of the 1.95 eV component, resulting in a more defined emission profile. The 1.97 eV emission is close to the optical band gap values obtained from the Tauc analysis, suggesting that this component is associated with near-band-edge radiative recombination. In contrast, the lower-energy component at 1.95 eV may be related to localized electronic states or shallow defect-related transitions reported for Cu-based oxide/chalcogenide semiconductors [46–49].

Hall measurements carried out at room temperature (Table 5) show that all Cu–Se–O films behave as p-type semiconductors. This tendency is not unusual for copper-based oxides and chalcogenides and is often linked to the presence of acceptor-like defects in the structure. Electrical conductivity values span from 7.2×10^{-1} to 1.26×10^{4} ($\Omega^{-1}\cdot cm^{-1}$), which is consistent with semiconducting behavior. The mobility values are not constant from one sample to another and span a broad interval, from 11.9 up to 419.62 $cm^2/V\cdot s$. The lowest mobility is associated with the F1-PLD film, where the surface is mainly formed by nanoflake-like features. In contrast, the F2-PLD sample, characterized by the presence of nanorods, shows a much higher mobility.

Table 5
Electrical properties of Cu-Se-O system thin films obtained by PLD.

Id Sample	Thickness (nm)	Bulk Concentration (cm^{-3})	Mobility ($cm^2/V\bullet s$)	Sheet Resistance ($\varvec{\Omega}/\square$)	Resistivity ($\varvec{\Omega}\bullet cm$)	Conductivity ($1/\varvec{\Omega}\bullet cm$)
F1-PLD	185	9.18×10^{20}	11.9	3.1×10^{1}	5.7×10^{-4}	1.75×10^{3}
F2-PLD	141	1.07×10^{16}	419.6	9.9×10^{4}	1.39	7.2×10^{-1}
F3-PLD	150	1.86×10^{21}	42.4	5.3	7.9×10^{-5}	1.26×10^{4}

Rather than being a simple variation, this difference seems to follow the changes in morphology observed by SEM. More elongated structures appear to facilitate charge transport, while more fragmented surfaces tend to limit it. In this context, copper vacancies are frequently considered when discussing p-type conductivity in these systems, as they can act as acceptor centers. This interpretation is consistent with the trends suggested by the chemical potential analysis [29].

The resulting carrier concentrations, ranging from 10^{16} to 10^{21} cm^{-3}, are in good agreement with values previously reported for p-type oxide–chalcogenide materials deposited by PLD. Samanta et al. [45] reported similar carrier concentrations and mobilities in semiconducting oxides, attributing this behavior to the presence of acceptor-type defects.

4 Conclusions

Cu–Se–O oxychalcogenide powders were obtained by high-energy ball milling at different milling times and subsequently used as precursors for the deposition of thin films by PLD. At 6 h of milling, the powder exhibited an elemental composition of 36.44 at.% O, 33.28 at.% Cu, and 30.28 at.% Se, as determined by EDS. All PLD films showed an increase in oxygen content, while the elemental composition indicated a loss of Cu for the films prepared using the powders milled for 2 and 4 h. The film prepared with the powder milled during 6 h exhibited a single-phase $Cu_4O(SeO_3)_3$ structure. XRD analysis showed that the crystalline structure of F3-PLD corresponded to single-phase $Cu_4O(SeO_3)_3$, with crystallite sizes ranging from approximately 21.7 to 32.8 nm.

The SEM analysis showed that the structural changes were accompanied by pronounced variations in the surface microstructure. F1-PLD exhibited nanoparticle coalescence together with nanoflake-like features, F2-PLD presented interconnected nanorods, and F3-PLD evolved toward a more homogeneous surface composed mainly of semispherical nanoparticles. The Raman spectra showed variations in the Cu–Se–O vibrational features with increasing ball-milling time and after deposition as thin films.

Optical transmission measurements yielded band gap values in the range of 1.8–2.0 eV, while the PL response changed from a broad emission centered at 1.78 eV for F1-PLD to more defined emissions at 1.95 and 1.97 eV for both F2-PLD and F3-PLD. Hall measurements indicated p-type conductivity for all films, with carrier concentrations ranging from 1.07×10^{16} to 1.86×10^{21} cm^{-3} and mobilities between 11.9 and 419.6 $cm^2/V{\cdot}s$. The resulting electrical conductivity therefore varied substantially among the films, reflecting the combined contribution of carrier concentration and mobility.

Overall, the combination of high-energy ball milling and PLD allows the preparation of Cu–Se–O thin films with different structural and optoelectronic characteristics. The solvent-free processing of the precursor powders and their direct use for PLD deposition provide a practical approach for preparing Cu–Se–O thin films without solution-based precursor processing. The obtained results provide a basis for further investigation of these materials as semitransparent p-type oxychalcogenides for optoelectronic applications.

Declarations

Data availability

All the information to develop the work and the data obtained in this work were included in the manuscript

Acknowledgments

J. A. Melchor-Robles and Jacobo Martínez-Reyes thanks the financial support received from SECIHTI-México. “Estancias Posdoctorales Iniciales, convocatoria 2025”.

All authors express their gratitude to SECIHTI-México for the financial support provided to carry out this project.

The authors acknowledge the technical support from: M.A Luna Arias, A. Tavira Fuentes, Miguel Galvan Arellano, Marcela Guerrero, Ángel Guillen and A. Garcia Sotelo (CINVESTAV-IPN).

Funding

This work was supported by **SECIHTI**, 2025. The authors declare no competing financial interests.

Authors and Affiliations

Departamento de Física. CINVESTAVIPN, Ciudad de México, Instituto Politécnico Nacional 2508, San Pedro Zacatenco, Gustavo A. Madero, 07360, Ciudad de México, CDMX.

J. A. Melchor-Robles

Departamento de Ingeniería Eléctrica- SEES. CINVESTAV-IPN. Instituto Politécnico Nacional 2508, San Pedro Zacatenco, Gustavo A. Madero, 07360, Ciudad de México, CDMX.

Jacobo Martínez-Reyes

Laboratorio de Óptica e Informática, Universidad Popular del Cesar, Valledupar, Cesar 200001, Colombia

Edgar David Peduzine Orozco

Instituto Politécnico Nacional, Unidad Profesional Adolfo López Mateo, Av. Miguel Bernard S/N, Col. Zacatenco, Del. Gustavo A. Madero, C.P. 07738, CDMX.

Tatiana Nayeli Domínguez Mendoza

5Escuela Superior de Ingeniería y Arquitectura Unidad Zacatenco, Instituto Politécnico Nacional (ESIAZ-IPN), Unidad Profesional Adolfo López Mateo, Av. Miguel Bernard S/N, Col. Zacatenco, Del. Gustavo A. Madero, C.P. 07738, Ciudad de México, México.

K. E. Nieto-Zepeda

Facultad de Química, Energía-Materiales, Universidad Autónoma de Querétaro, Cerro de las Campanas S/N, Las Campanas, 76010 Santiago de Querétaro, Qro.

Francisco Javier de Moure Flores

Departamento de Ingeniería Eléctrica- SEES. CINVESTAV-IPN. Instituto Politécnico Nacional 2508, San Pedro Zacatenco, Gustavo A. Madero, 07360, Ciudad de México, CDMX.

M. de la L. Olvera

Departamento de Física, Centro de Investigación y de Estudios Avanzados del IPN, Ciudad de México. Instituto Politécnico Nacional 2508, San Pedro Zacatenco, Gustavo A. Madero, 07360, Ciudad de México, CDMX.

Miguel Ángel Meléndez Lira

Contributions

All authors have contributed to the manuscript. JAMR: wrote the original draft as well as the editing and corrections. JMR: contributed to the experimental development methodology. EDPO, TNDM and KENZ: contributed during analysis and investigation. FJDF and MLOA: provided resources, supervision, and validation. MAML: data Visualization, Verification and review.

Corresponding author

Correspondence to: Jacobo Martinez Reyes, jacobo.martinez.r@cinvestav.mx

Ethics declarations

Conflict of interest

The authors declare that they have no known competing financial interests or personal relationships that could have appeared to influence the work reported in this paper.

References

1. N. Zhang, J. Sun, H. Gong, Transparent p-Type Semiconductors: Copper-Based Oxides and Oxychalcogenides, *Coatings*, vol. 9, no. 2, p. 137, Feb. 2019, 10.3390/coatings9020137
2. E. Flores-Rojas, J.E. Samaniego-Benítez, R. Serrato, A. García-García, R. Ramírez-Bon, J. Ramírez-Aparicio, Transformation of Nanostructures Cu_2O to Cu_3Se_2 through Different Routes and the Effect on Photocatalytic Properties, *ACS Omega*, vol. 5, no. 32, pp. 20335–20342, Aug. 2020, 10.1021/acsomega.0c02299
3. F.A.C.C.H.E.T.T.I. ANTONIO, *Transparent Electronics: From Synthesis to Applications* (Wiley, 2010)
4. R.W. Lord, J. Fanghanel, C.F. Holder, I. Dabo, R.E. Schaak, Colloidal Nanoparticles of a Metastable Copper Selenide Phase with Near-Infrared Plasmon Resonance, *Chemistry of Materials*, vol. 32, no. 23, pp. 10227–10234, Dec. 2020, 10.1021/acs.chemmater.0c04058

5. C.M. Hessel et al., Jun., Copper Selenide Nanocrystals for Photothermal Therapy, *Nano Lett.*, vol. 11, no. 6, pp. 2560–2566, 2011, 10.1021/nl201400z
6. R. Zhou et al., Copper selenide (Cu_3Se_2 and $Cu_{2-x}Se$) thin films: electrochemical deposition and electrocatalytic application in quantum dot-sensitized solar cells. Dalton Trans. **47**(46), 16587–16595 (2018). 10.1039/C8DT03791D
7. S. Thirumavalavan, K. Mani, S. Sagadevan, Investigation of the Structural, Optical and Electrical Properties of Copper Selenide Thin Films, *Materials Research*, vol. 18, no. 5, pp. 1000–1007, Oct. 2015, 10.1590/1516-1439.039215
8. D. Shi, Z. Geng, L. Shi, Y. Li, K. Lam, Thermal stability study of $Cu_{1.97}Se$ superionic thermoelectric materials. J. Mater. Chem. C Mater. **8**(30), 10221–10228 (2020). 10.1039/D0TC01085E
9. S.L. White, P. Banerjee, P.K. Jain, Liquid-like cationic sub-lattice in copper selenide clusters. Nat. Commun. **8**(1), 14514 (Apr. 2017). 10.1038/ncomms14514
10. P. Roy, S.K. Srivastava, Nanostructured copper sulfides: synthesis, properties and applications. CrystEngComm. **17**, 7801–7815 (2015). 10.1039/C5CE01304F
11. C.-T. Yang, H.-I. Hsiang, J.-H. Tu, Copper selenide crystallites synthesized using the hot-injection process. Adv. Powder Technol. **27**(3), 959–963 (May 2016). 10.1016/j.apt.2016.03.004
12. E.M. Williamson, Z. Sun, B.A. Tappan, R.L. Brutchey, Predictive Synthesis of Copper Selenides Using a Multidimensional Phase Map Constructed with a Data-Driven Classifier, *J. Am. Chem. Soc.*, vol. 145, no. 32, pp. 17954–17964, Aug. 2023, 10.1021/jacs.3c05490
13. D.J. Chakrabarti, D.E. Laughlin, The Cu – Se (Copper-Selenium) system, *Bulletin of Alloy Phase Diagrams*, vol. 2, no. 3, pp. 305–315, Dec. 1981, 10.1007/BF02868284
14. R.D. Heyding, THE COPPER/SELENIUM SYSTEM. Can. J. Chem. **44**(10), 1233–1236 (May 1966). 10.1139/v66-183
15. R.D. Heyding, R.M. Murray, The crystal structures of $Cu_{1.8}Se$, Cu_3Se_2, α- and γCuSe, $CuSe_2$, and $CuSe_2$ II, *Can. J. Chem.*, vol. 54, no. 6, pp. 841–848, Mar. 1976, 10.1139/v76-122
16. L. Xue et al., Mar., Thermoelectric performance of Cu2Se bulk materials by high-temperature and high-pressure synthesis, *Journal of Materiomics*, vol. 5, no. 1, pp. 103–110, 2019, 10.1016/j.jmat.2018.12.002
17. K. Ueda, K. Takafuji, H. Hosono, Preparation and crystal structure analysis of CeCuOS. J. Solid State Chem. **170**(1), 182–187 (Jan. 2003). 10.1016/S0022-4596(02)00061-0
18. A. Ali, Y.W. Chiang, R.M. Santos, X-ray Diffraction Techniques for Mineral Characterization: A Review for Engineers of the Fundamentals, Applications, and Research Directions. Minerals. **12**(2), 205 (Feb. 2022). 10.3390/min12020205
19. S. Ahmed et al., Crystallinity integration of anatase (TiO2) nanocrystal by whole powder pattern fitting (WPPF) method: A Rietveld refinement study. Results Mater. **26**, 100673 (Jun. 2025). 10.1016/j.rinma.2025.100673

20. K. Kohn, K. Inoue, O. Horie, S.-I. Akimoto, Crystal chemistry of MSeO3 and MTeO3 (M = Mg, Mn, Co, Ni, Cu, and Zn). J. Solid State Chem. **18**(1), 27–37 (May 1976). 10.1016/0022-4596(76)90075-X
21. K. Kohn, S. Akimoto, K. Inoue, K. Asai, O. Horie, Crystal Structure and Magnetic Properties of $MnSeO_3$, $CoSeO_3$, $NiSeO_3$ and $CuSeO_3$, *J. Physical Soc. Japan*, vol. 38, no. 2, pp. 587–587, Feb. 1975, 10.1143/JPSJ.38.587
22. H. Effenberger, F. Pertlik, Die Kristallstrukturen der Kupfer(II)-oxo-selenite Cu2O(SeO3) (kubisch und monoklin) und Cu4O(SeO3)3 (monoklin und triklin). Monatshefte f□r Chemie Chem. Monthly. **117**, 8–9 (1986). 10.1007/BF00811258
23. A.H. Goldan, C. Li, S.J. Pennycook, J. Schneider, A. Blom, W. Zhao, Molecular structure of vapor-deposited amorphous selenium. J. Appl. Phys. **120**(13) (Oct. 2016). 10.1063/1.4962315
24. K. Mubeen et al., ZnO/CuS nanocomposites for efficient visible light-driven degradation of methylene blue: mechanisms and performance evaluation. J. Mater. Sci.: Mater. Electron. **36**, 992 (Jun. 2025). 10.1007/s10854-025-15014-4
25. Y. Deng, A.D. Handoko, Y. Du, S. Xi, B.S. Yeo, *In Situ* Raman Spectroscopy of Copper and Copper Oxide Surfaces during Electrochemical Oxygen Evolution Reaction: Identification of Cu^{III} Oxides as Catalytically Active Species. ACS Catal. **6**(4), 2473–2481 (Apr. 2016). 10.1021/acscatal.6b00205
26. Y. Liu et al., Ball-milling-induced lattice distortion in Cu2O catalysts for the direct synthesis of tetramethoxysilane from methanol and silicon. Mol. Catal. **589**, 115610 (Feb. 2026). 10.1016/j.mcat.2025.115610
27. M. Achimovičová et al., Comparative Study of Nanostructured CuSe Semiconductor Synthesized in a Planetary and Vibratory Mill, *Nanomaterials*, vol. 10, no. 10, p. 2038, Oct. 2020. 10.3390/nano10102038
28. V.M. Kovrugin et al., Synthesis and crystal structure of β-CuSe2O5, a new polymorph of copper diselenite. Mendeleev Commun. **27**(1), 61–63 (Jan. 2017). 10.1016/j.mencom.2017.01.019
29. A. Arakcheeva, P.R. Baral, W.H. Bi, C. Jandl, O. Janson, A. Magrez, Cu_2OSeO_3 turns trigonal with structural transformation and implications for skyrmions. Sci. Rep. **15**(1), 31945 (Aug. 2025). 10.1038/s41598-025-15886-w
30. G. Petretto et al., High-throughput density-functional perturbation theory phonons for inorganic materials. Sci. Data. **5**(1), 180065 (Dec. 2018). 10.1038/sdata.2018.65
31. H. Yokokawa, Generalized chemical potential diagram and its applications to chemical reactions at interfaces between dissimilar materials. J. Phase Equilib. **20**(3), 258–287 (May 1999). 10.1361/105497199770335794
32. D.A. Clemente, A. Marzotto, The P1 space group changes in journal of crystallographic and spectroscopic research and in journal of chemical crystallography, *J. Chem. Crystallogr.*, vol. 33, no. 12, pp. 933–945, Dec. 2003, 10.1023/A:1027433915898
33. L. Li et al., Vertically Oriented and Interpenetrating CuSe Nanosheet Films with Open Channels for Flexible All-Solid-State Supercapacitors. ACS Omega. **2**(3), 1089–1096 (Mar. 2017). 10.1021/acsomega.6b00535

34. Y. Zhao et al., May., Speciation of Cu Surfaces During the Electrochemical CO Reduction Reaction, *J. Am. Chem. Soc.*, p. jacs.0c02354, 2020, 10.1021/jacs.0c02354
35. R.L. Frost, E.C. Keeffe, Raman spectroscopic study of the selenite minerals—chalcomenite $CuSeO_3 \cdot 2H_2O$, clinochalcomenite and cobaltomenite, *Journal of Raman Spectroscopy*, vol. 39, no. 12, pp. 1789–1793, Dec. 2008, 10.1002/jrs.2036
36. O. Ramirez, P. Ramasamy, Y. Chan Choi, J.-S. Lee, Morphology Transformation of Chalcogenide Nanoparticles Triggered by Cation Exchange Reactions. Chem. Mater. **31**(1), 268–276 (Jan. 2019). 10.1021/acs.chemmater.8b04550
37. J. Zhu, H. Wang, Synthesis of Metal Chalcogenide Nanoparticles. ChemInform. **35**(44) (Nov. 2004). 10.1002/chin.200444249
38. H. Raebiger, S. Lany, A. Zunger, Origins of the p-type nature and cation deficiency in C_2O and related materials. Phys. Rev. B **76**(4), 045209 (Jul. 2007). 10.1103/PhysRevB.76.045209
39. H. Kawazoe, M. Yasukawa, H. Hyodo, M. Kurita, H. Yanagi, H. Hosono, P-type electrical conduction in transparent thin films of CuAlO2, *Nature*, vol. 389, no. 6654, pp. 939–942, Oct. 1997, 10.1038/40087
40. M. Moreira, J. Afonso, J. Crepelliere, D. Lenoble, P. Lunca-Popa, A review on the p-type transparent Cu–Cr–O delafossite materials. J. Mater. Sci. **57**(5), 3114–3142 (Feb. 2022). 10.1007/s10853-021-06815-z
41. J. Tauc, R. Grigorovici, A. Vancu, Optical Properties and Electronic Structure of Amorphous Germanium. Phys. status solidi (b). **15**(2), 627–637 (Jan. 1966). 10.1002/pssb.19660150224
42. B.D. Viezbicke, S. Patel, B.E. Davis, D.P. Birnie, Evaluation of the Tauc method for optical absorption edge determination: ZnO thin films as a model system, *physica status solidi (b)*, vol. 252, no. 8, pp. 1700–1710, Aug. 2015, 10.1002/pssb.201552007
43. C. Chen, X. Lai, H. Liu, Z. Weng, D. Ge, Y. Huang, Facile one-pot synthesis of high-purity crystalline Cu4O(SeO3)3: Structural insights and characterization, *J. Solid State Chem.*, vol. 350, p. 125489, Oct. 2025, 10.1016/j.jssc.2025.125489
44. I.G. Shitu, Z.A. Talib, J.L.Y. Chi, M.M.A. Kechick, H. Baqiah, Influence of tartaric acid concentration on structural and optical properties of CuSe nanoparticles synthesized via microwave assisted method. Results Phys. **17**, 103041 (Jun. 2020). 10.1016/j.rinp.2020.103041
45. N.N. Krishnan, S. Vijayakumar, P. Gnanadurai, R. Shabu, K.C. Preetha, Structural and Optical Characterization of Copper Selenide (Cu2-XSe) Nanoparticles. J. Nanosci. Technol. **04**(02), 345–347 (Apr. 2018). 10.30799/jnst.sp204.18040202
46. S.M. Ali, H.K. Hassun, A.A. Salih, R.H. Athab, B.K.H. Al-Maiyaly, B.H. Hussein, Study the properties of Cu2Se thin films for optoelectronic applications, *Chalcogenide Letters*, vol. 19, no. 10, pp. 663–671, Oct. 2022
47. N.K. Abbas, A.A. Baker, N.J. Ghdeeb, The Effect of annealing temperature on the optical properties of $(Cu_2S)_{100-x}(SnS_2)_x$ thin films. Baghdad Sci. J. **11**(2), 641–651 (Jun. 2014). 10.21123/bsj.11.2.641-651

48. M. Petrovic et al., Optical properties of CuSe thin films - band gap determination. Sci. Sinter. **49**(2), 167–174 (2017). 10.2298/SOS1702167P
49. W. Lee, N. Myung, K. Rajeshwar, C.-W. Lee, Electrodeposition of Cu_2Se Semiconductor Thin Film on Se-Modified Polycrystalline Au Electrode, *Journal of Electrochemical Science and Technology*, vol. 4, no. 4, pp. 140–145, Dec. 2013, 10.5229/JECST.2013.4.4.140

Figures

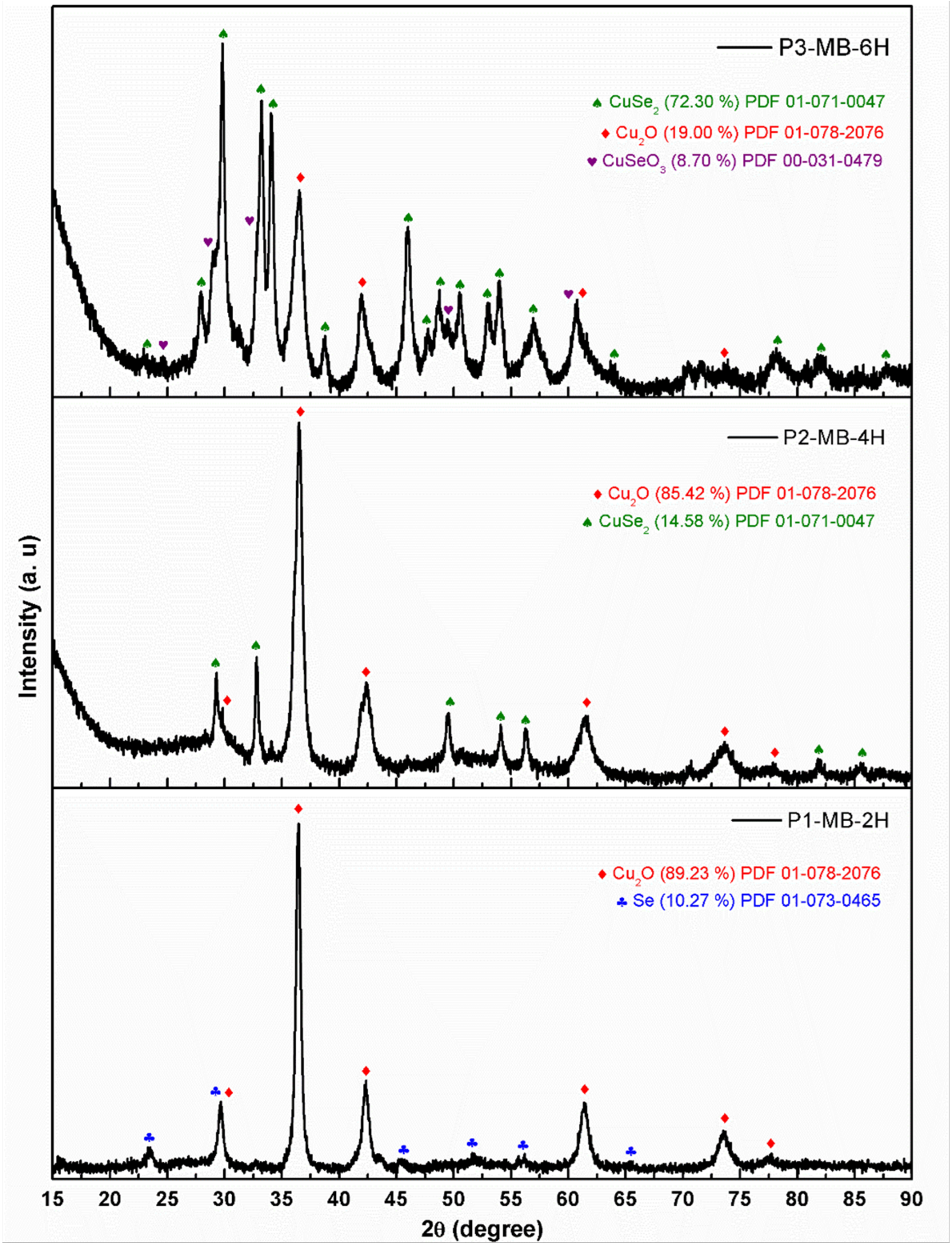


Figure 1

A) XRD patterns of the Cu–Se–O system obtained at different milling times.

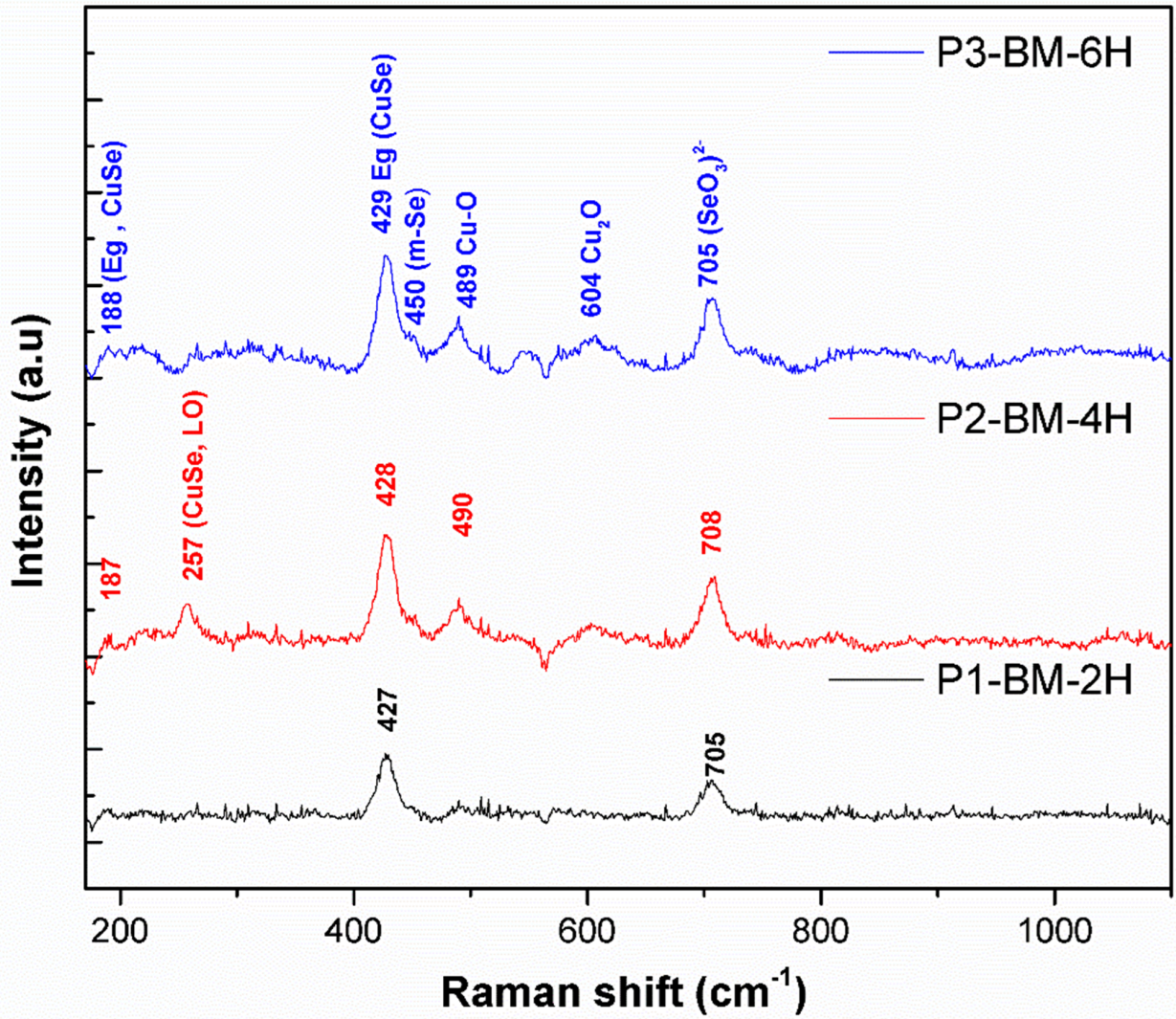


Figure 2

Raman spectra of Cu–Se–O powders synthesized by BM at different milling times, showing characteristic vibrational modes associated with Cu–Se, Cu–O, and Se–O bonds.

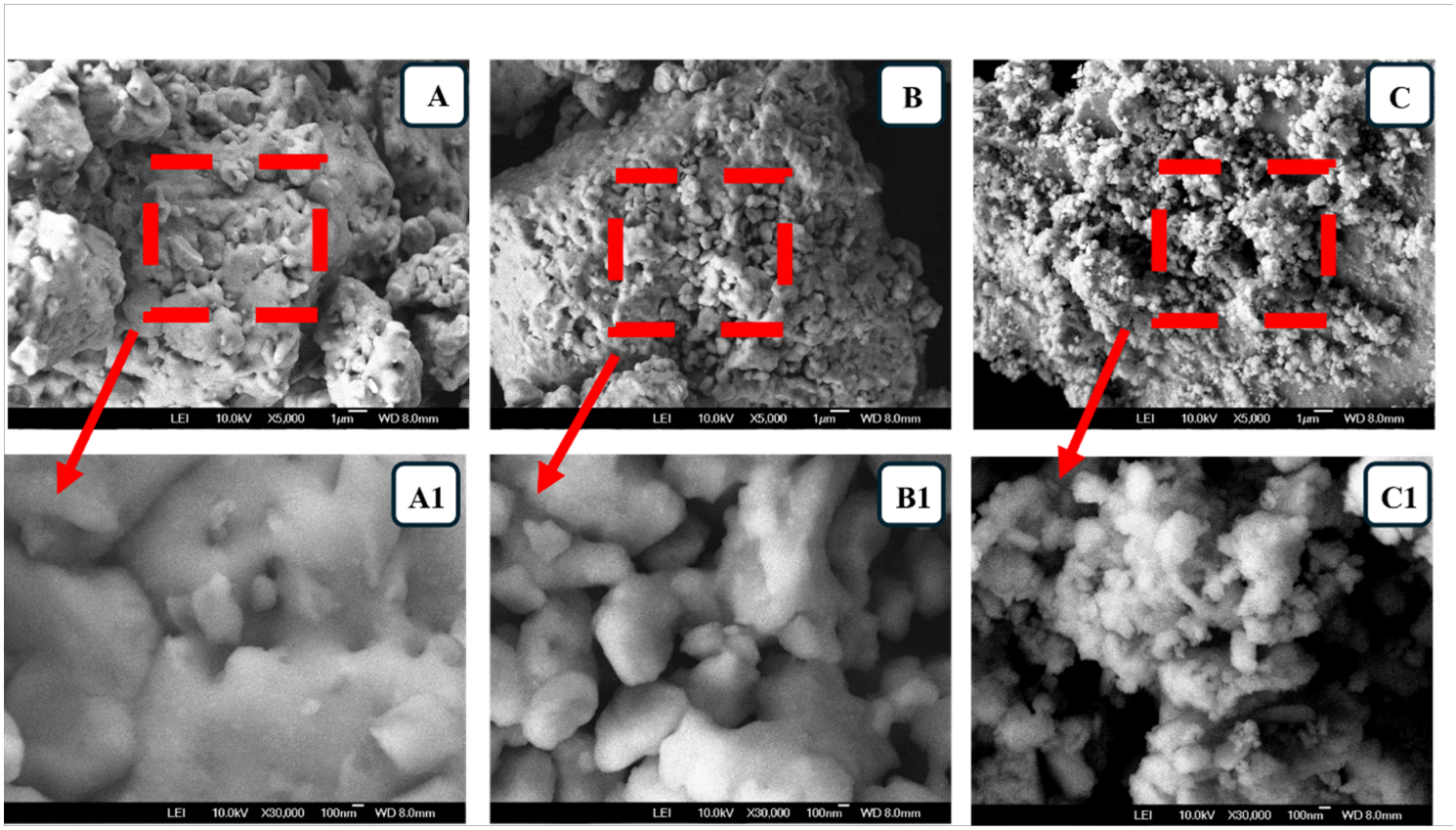


Figure 3

SEM analyses of Cu–Se–O powders synthesized by BM. (A) P1-BM-2H, (B) P2-BM-4H, and (C) P3-BM-6H.

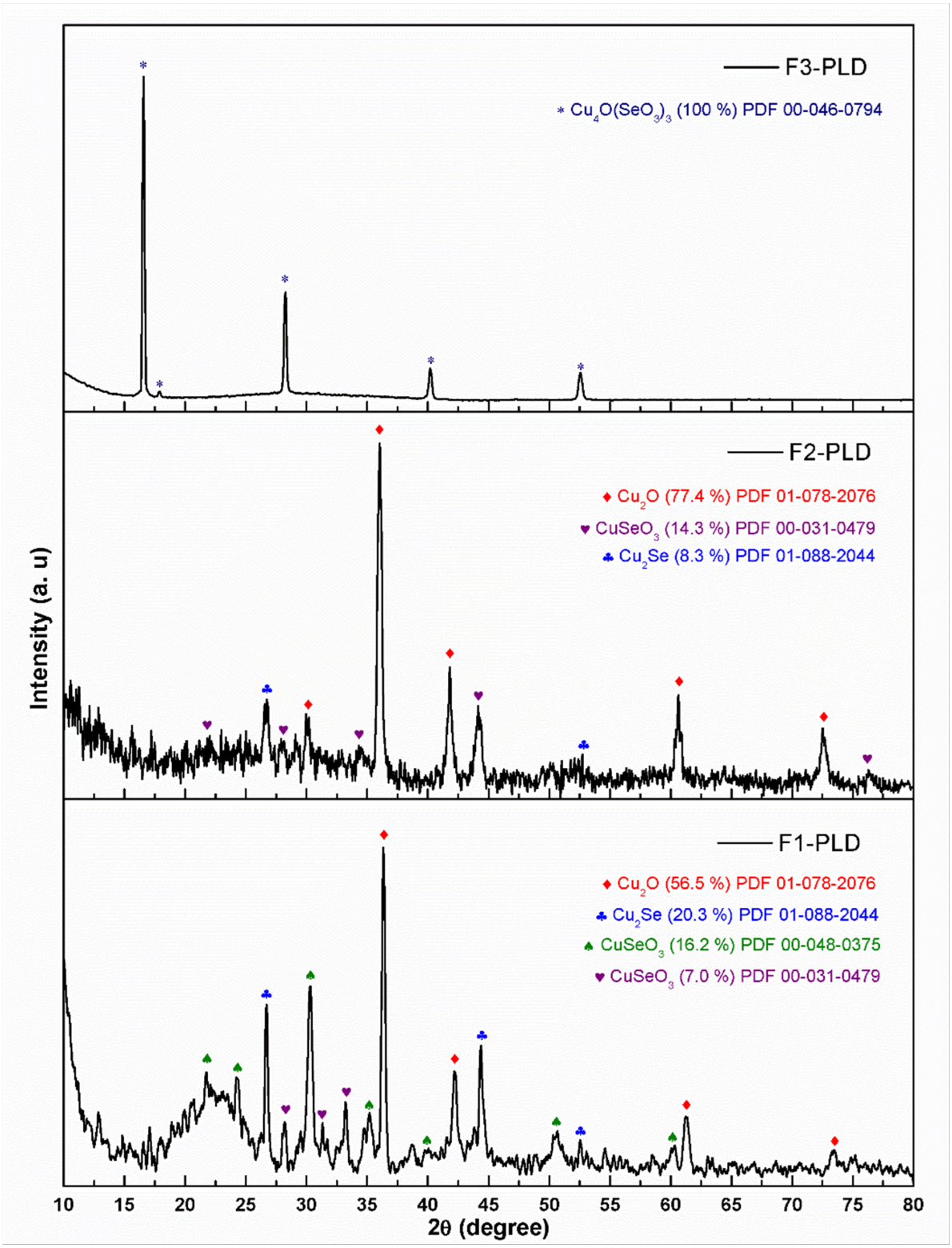


Figure 4

XRD patterns of Cu–Se–O thin films deposited by PLD from targets prepared at different milling times.

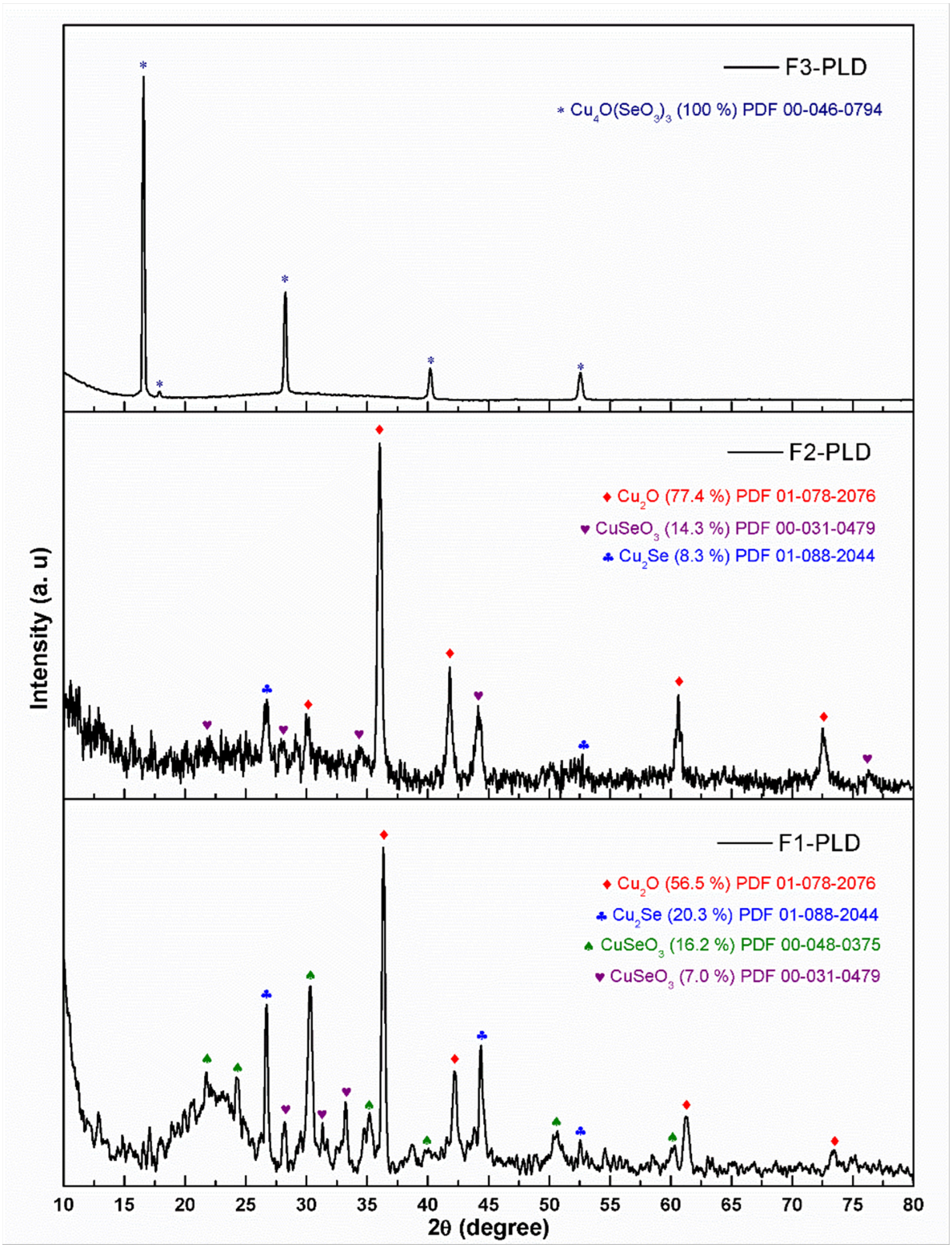


Figure 4

XRD patterns of Cu–Se–O thin films deposited by PLD from targets prepared at different milling times.

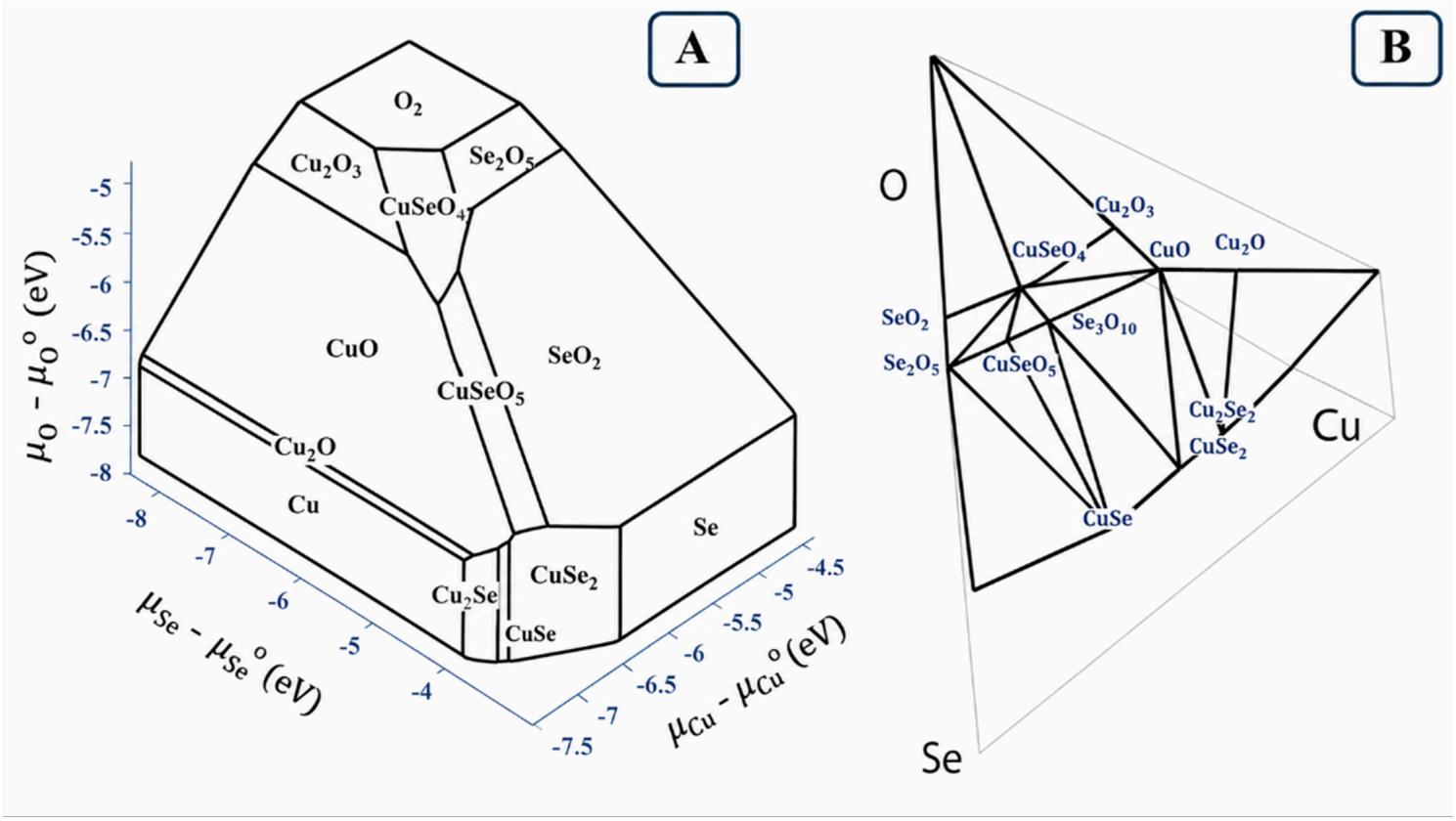


Figure 5

Chemical potential diagrams of the Cu–Se–O system: (A) chemical potential diagram and (B) theoretical phase diagram estimated at 300 K.

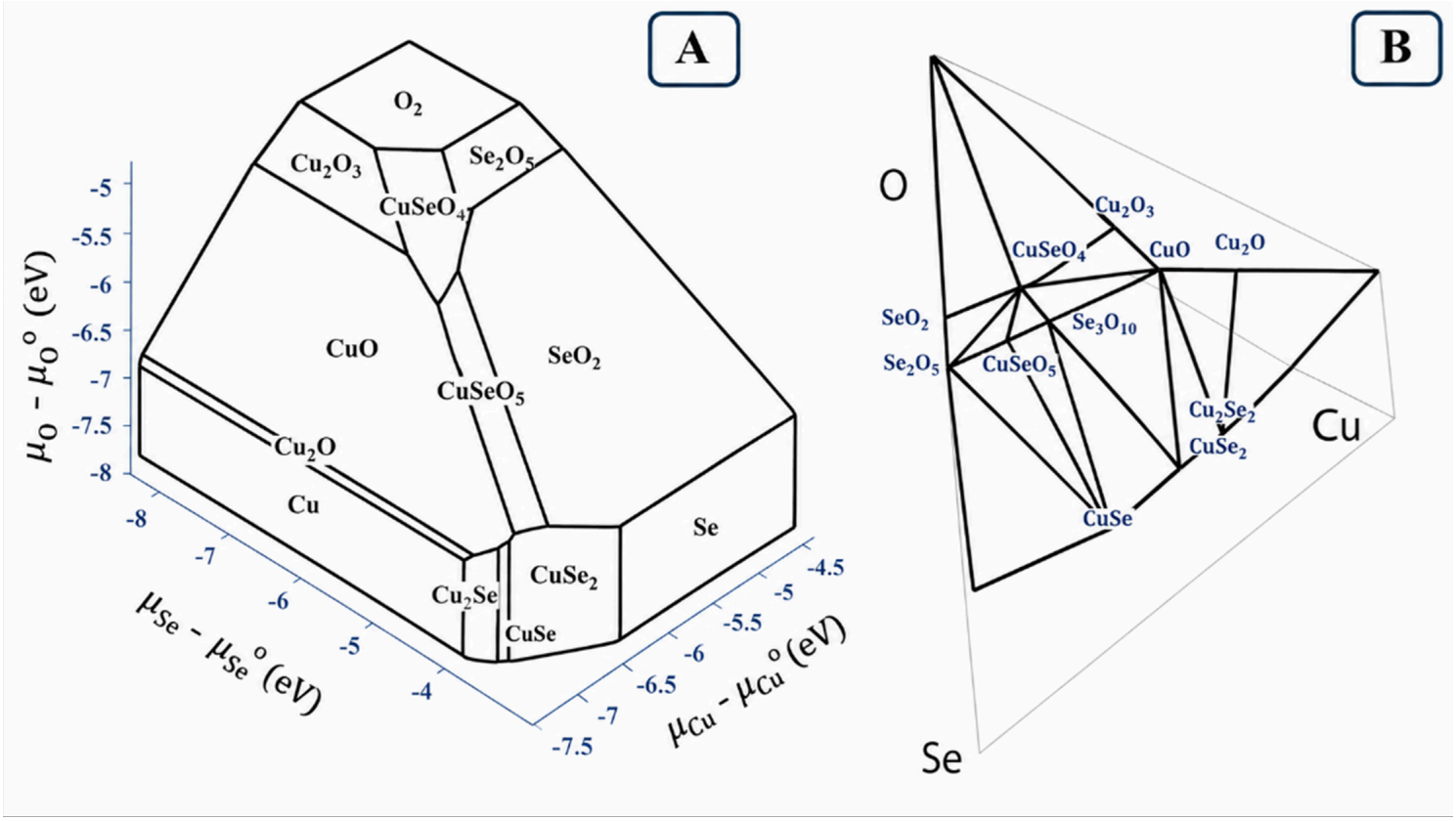


Figure 5

Chemical potential diagrams of the Cu–Se–O system: (A) chemical potential diagram and (B) theoretical phase diagram estimated at 300 K.

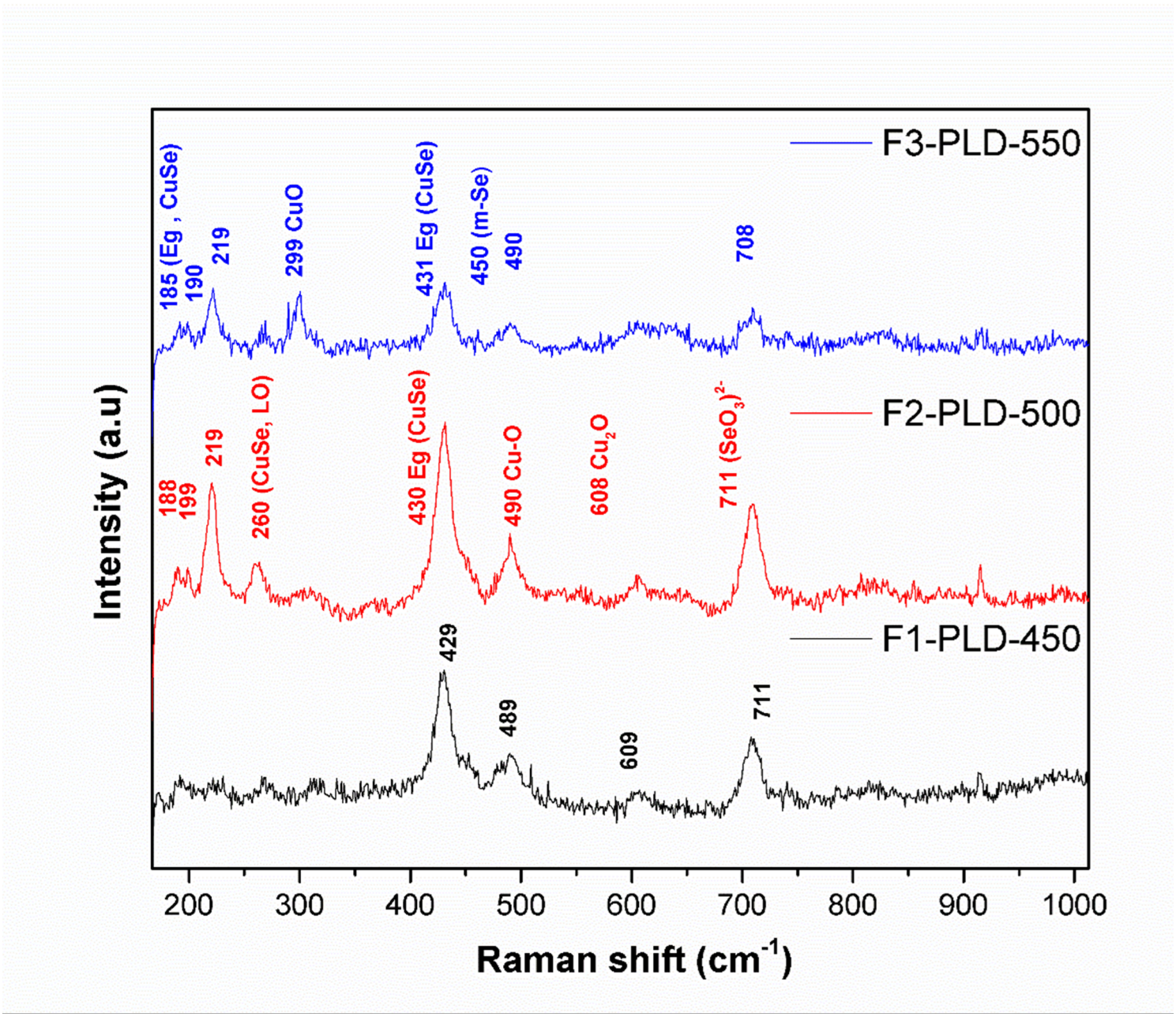


Figure 6

Raman spectra of Cu–Se–O thin films deposited by PLD for samples F1-PLD, F2-PLD, and F3-PLD, showing characteristic vibrational modes associated with Cu–Se, Cu–O, and Se–O bonds.

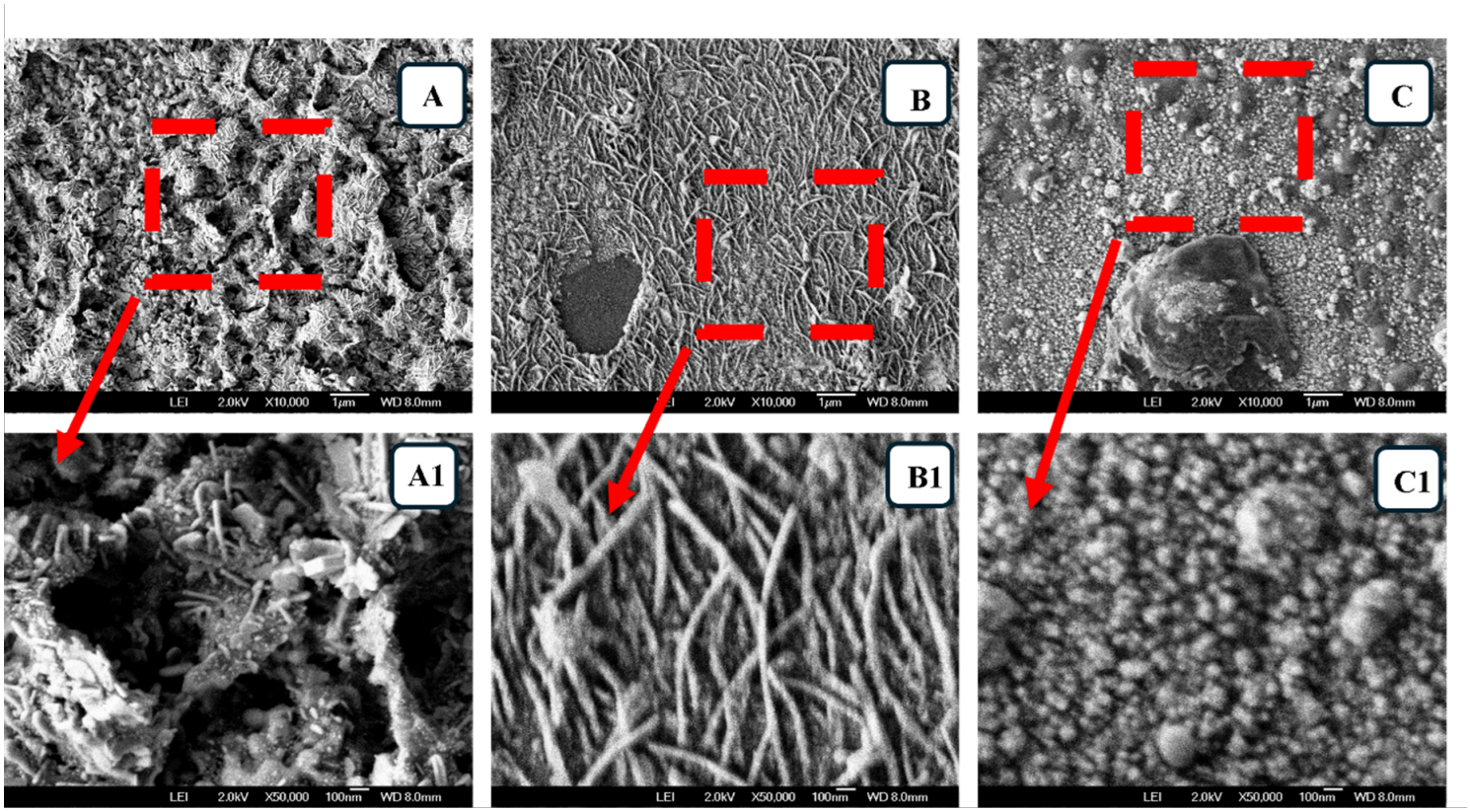


Figure 7

SEM analysis of Cu–Se–O thin films deposited by PLD: (A) F1-PLD, (B) F2-PLD, and (C) F3-PLD.

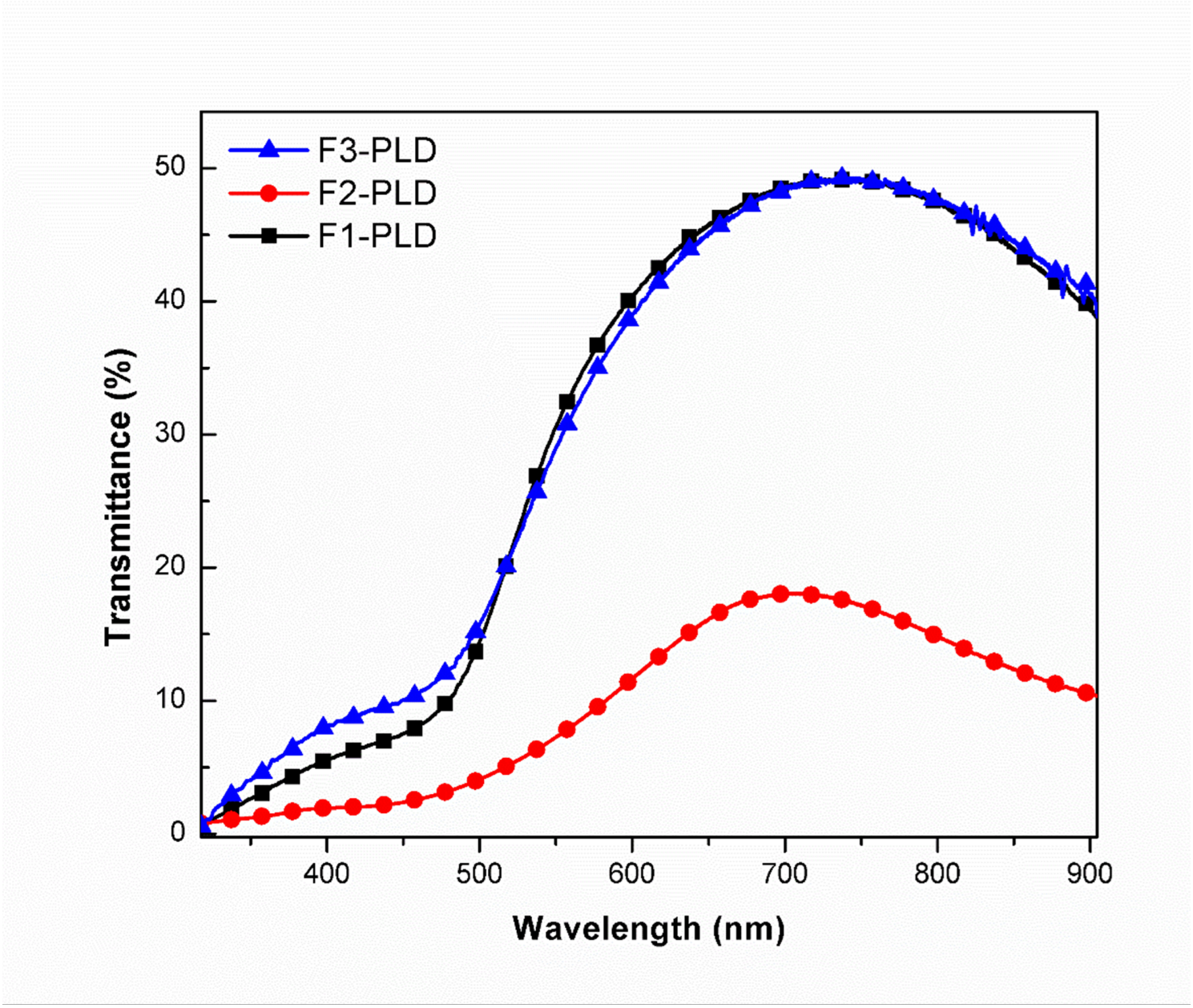


Figure 8

Optical transmittance spectra of Cu–Se–O thin films deposited by PLD.

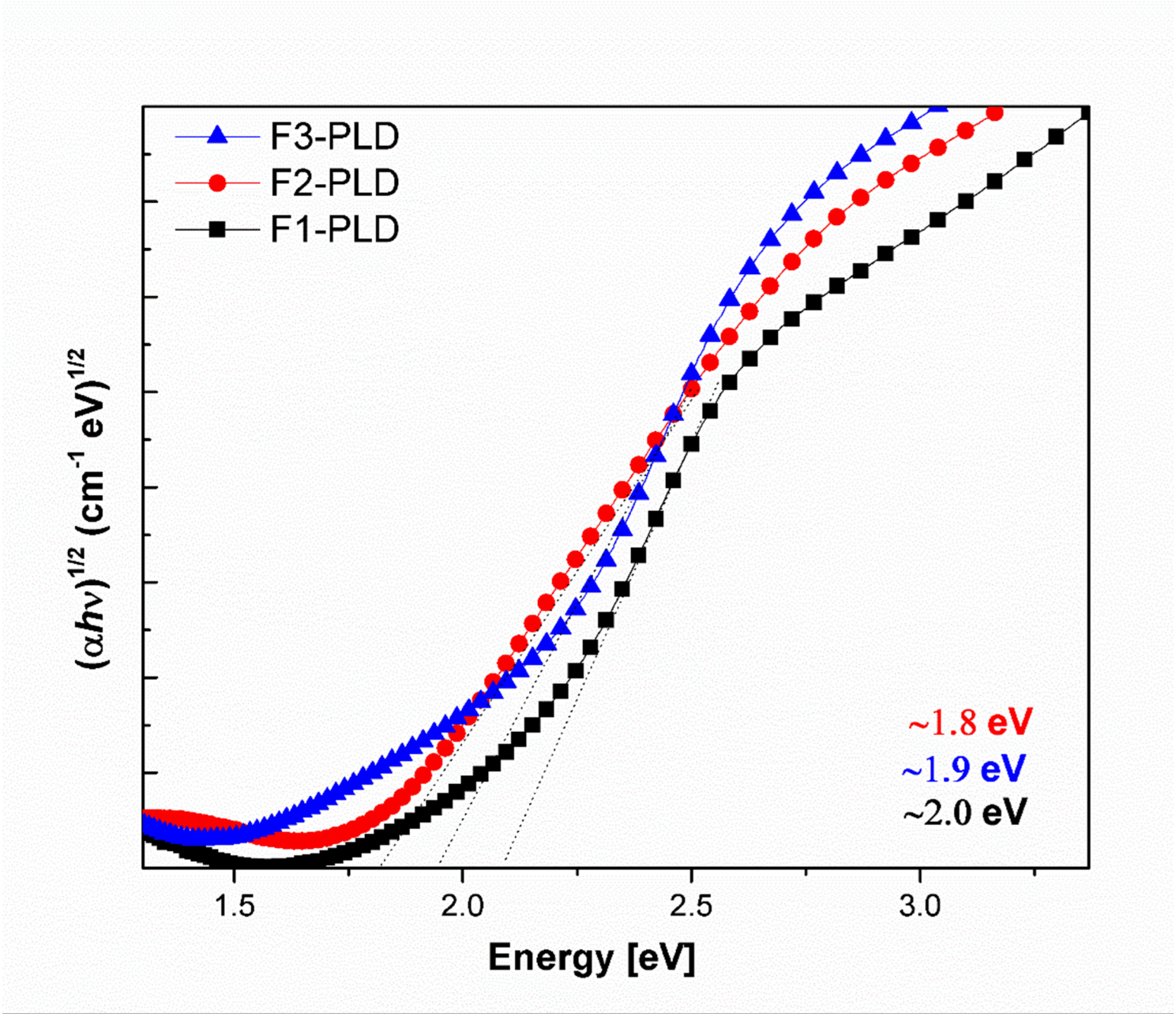


Figure 9

Optical band gap estimation of Cu–Se–O thin films obtained by PLD using the Tauc method: (A) F1-PLD, (B) F2-PLD, and (C) F3-PLD

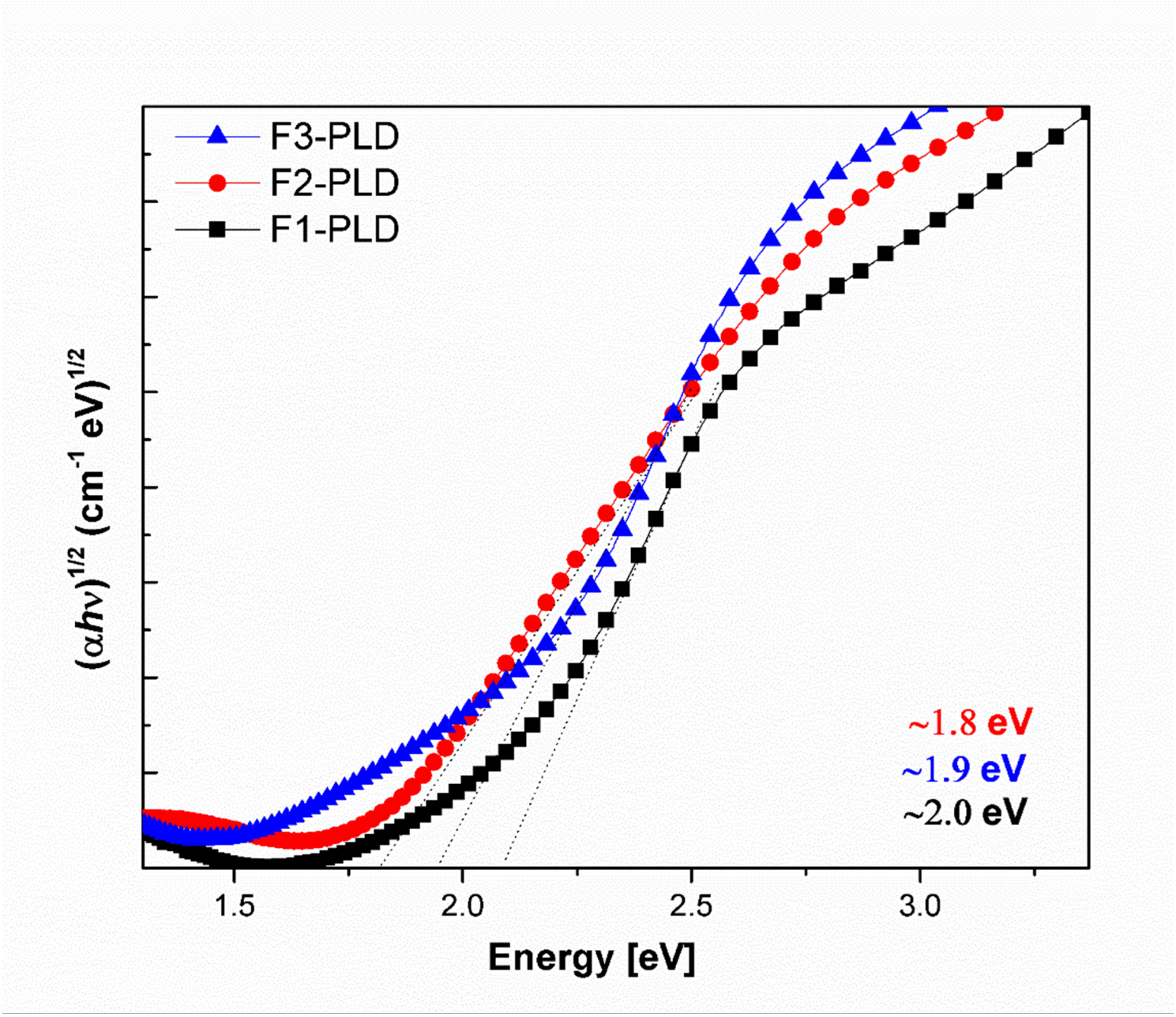


Figure 9

Optical band gap estimation of Cu–Se–O thin films obtained by PLD using the Tauc method: (A) F1-PLD, (B) F2-PLD, and (C) F3-PLD

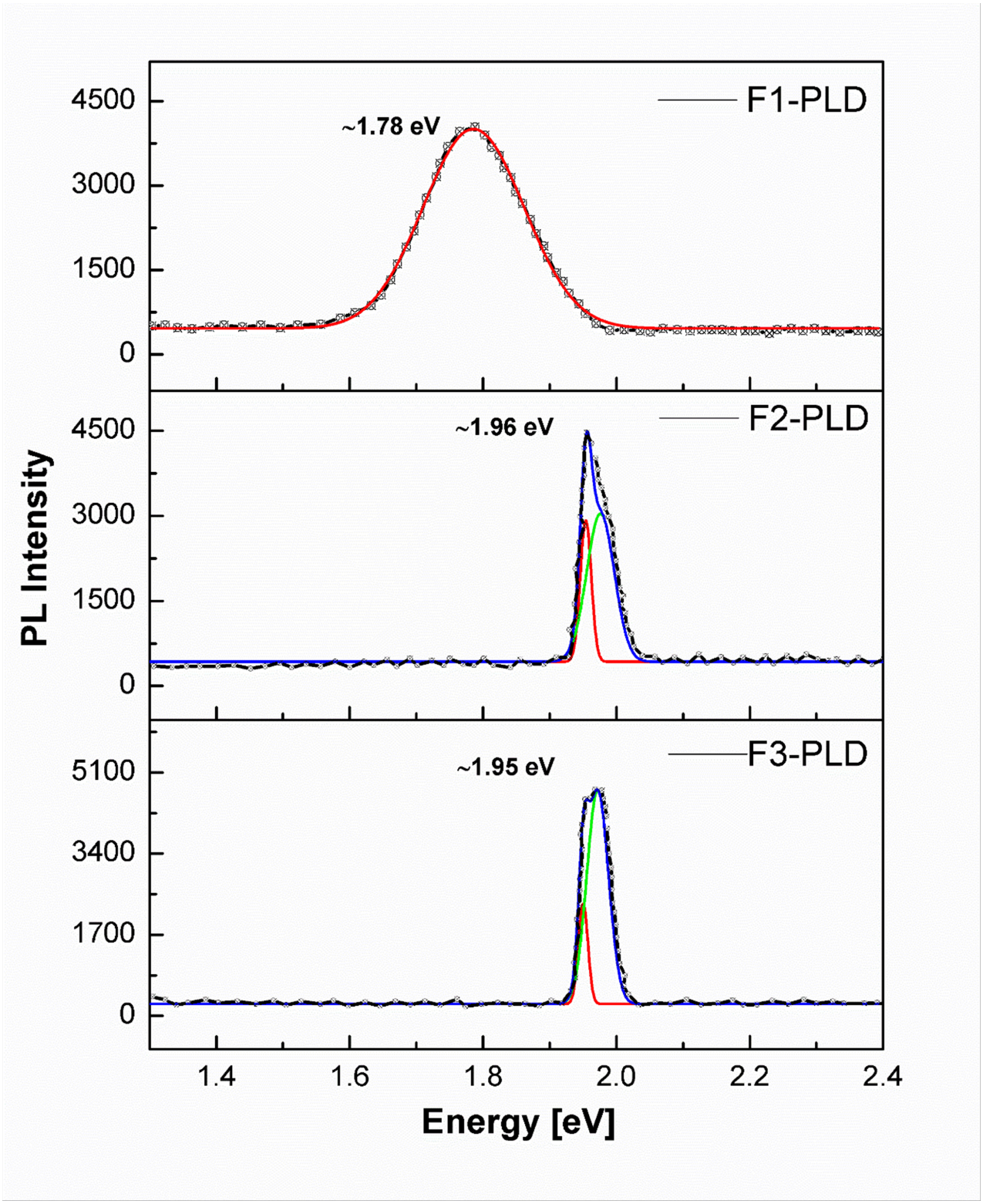


Figure 10

Photoluminescence (PL) spectra of Cu–Se–O thin films deposited by PLD for samples F1-PLD, F2-PLD, and F3-PLD.